Advances in Engineering Research : Possibilities and Challenges
ISSN Print: 3079-5192
ISSN Online: 3079-5206
https://doi.org/10.63313/AERpc.9053

Simulation of Thermal Barrier Layer Effects on Cu/PI Structures for Flexible Film Antenna Fabrication

Guanghui Dong[1.2]. Shufeng Sun[1.2.*]. Dunzhu GeSang[3]. Jin Wang[1.2]. Fengyun Zhang[1.2] and Tao Wei[1.2]

[1]Discipline Innovation and Wisdom Introduction Base of High-end Laser Intelligent Manufacturing Technology and Equipment, Qingdao University of Technology, Qingdao 266525, China

[2]Shandong Provincial Key Laboratory of High-end Laser Manufacturing Technology and Equipment, Qingdao University of Technology, Qingdao 266525, China

[3]Science and Technology in Vacuum Technology and Physics Laboratory, Lanzhou Institute of Physics, Lanzhou 730000, China

*Corresponding authors: sunshufeng@qut.edu.cn

How to cite this paper: Dong, G. H., Sun, S. F., GeSang, D. Z., Wang, J., Zhang, F. Y., & Wei, T. (2025). Simulation of Thermal Barrier Layer Effects on Cu/PI Structures for Flexible Film Antenna Fabrication. Advances in Engineering Research: Possibilities and Challenges, 2(3), 12–26. ISSN Print: 3079-5192; ISSN Online: 3079-5206. https://doi.org/10.63313/AERpc.9053
Published: 2025-10-23

Abstract

This study investigates the influence of a thermal barrier layer on the laser ablation behavior of a Cu/Ti/PI trilayer structure using finite element simulation in COMSOL Multiphysics. A 2D model was established to analyze the temperature distribution and material removal under nanosecond pulsed laser irradiation. The effects of single-pulse energy, thermal barrier layer thickness, pulse width, and scanning speed were systematically evaluated. Results indicate that a Ti thermal barrier layer with a thickness of 200 – 300 nm effectively delays the vaporization of the PI substrate while maintaining adequate copper removal. Optimal processing parameters were identified as a single-pulse energy of 450 μJ, pulse width of 120 ns, and scanning speed of 250 mm/s, which achieved complete copper ablation with minimal substrate damage.

Keywords

Laser Ablation; Thermal Barrier Layer; Finite Element Simulation; Cu/Ti/PI Structure; Nanosecond Laser

1. Introduction

The preparation of functional thin films on dielectric substrates to realize integrated structure-function components has been widely adopted in aerospace electromagnetics-for example in frequency-selective surfaces (FSS) and phased-array thin-film antennas[1-2]. By integrating conductive/functional films with low-loss dielectric foils, these platforms combine mechanical compliance with engineered RF responses, enabling lightweight and multifunctional apertures[3]. Depending on environmental loads, electrical performance targets, and structural design constraints, substrates are typically chosen from resin-based composites or organic films with high electromagnetic transparency-most notably polyimide (PI) and parylene. These polymers offer low permittivity and loss with excellent flexibility[4-5]. In typical fabrication flows, a conductive metal film (Cu/Ag/Al) is deposited on the polymer surface and subsequently patterned by photolithography and selective etching or, alternatively, by direct laser patterning, to precisely tailor the device's microwave transmission/reflection characteristics[6-7].

This manufacturing approach couples high-melting-point, high-reflectance metals with low-vaporization-threshold organics, creating a stack with strong thermophysical contrast. When multiple materials with distinct thermal/optical properties are co-processed, short-pulse etching becomes more intricate and can degrade edge quality or induce collateral damage[8]. Wang Rui et al.[9] studied the use of pulsed laser to etch metal films on organic material substrates. After laser etching metal films, they were directly irradiated to the surface of the material, which caused irreversible damage to the organic material substrates. To mitigate interfacial overheating and direct substrate damage, a thin thermal-barrier (sacrificial) interlayer can be introduced between the metal and PI to throttle through-thickness heat flow; Linden et al. showed such layers reduce recast and debris and improve hole quality in polymer–metal stacks[10]. Moreever, laser parameters exert a first-order influence on etch quality and selectivity, The research by Hribar[11], and He[12] et al. has investigated the influence of parameters such as laser pulse energy, pulse width, and scanning speed on etching quality.

The metal layer thickness of thin-film antennas must be at least three times the skin depth at the operating frequency. For this study, a 3 μm thick copper film was chosen, which satisfies the requirements for antennas operating in the 1–30 GHz range[13]. Given the sub-microsecond timescales and coupled transport during nanosecond processing, direct measurement of transient interfacial temperature is challenging. We therefore employ COMSOL Multiphysics finite-element analysis to simulate metal/thermal-barrier/PI—solving for Gaussian-beam absorption and transient conduction to estimate peak temperatures in the metal, interface, and polymer. The simulations identify safe processing windows to ensure complete metal removal while preventing direct laser irradiation of the PI substrate and postponing its vaporization, enabling optimization of pulse energy, pulse width and overlap rate.

2. Finite Element Model

2.1. Model Construction

Using COMSOL Multiphysics software, a three-layer structure comprising PI substrate, a thermal barrier layer and Cu film finite element models was established, as illustrated in Figure 1. A thermal barrier layer was introduced between the Cu film and PI substrate. Titanium (Ti) and chromium (Cr)—both high-melting-point, low-thermal-conductivity materials—were considered. Ti was ultimately selected due to its significantly lower thermal conductivity than Cr, which promotes a steeper temperature gradient and better mitigates heat transfer to the PI substrate. Additionally, Ti exhibits excellent compatibility with Cu and PI, is widely used as an adhesion layer, and does not react detrimentally with PI during laser processing [14-15].

A two-dimensional model of a Cu/Ti/PI trilayer structure with a width of 120 μm was constructed (see Figure 1). The model consisted of a 50 μm-thick polyimide (PI) substrate and a 3 μm thick copper film.

This model was imported into COMSOL Multiphysics for transient analysis. A laser beam with a wavelength of 1064 nm was vertically incident on the metal film surface, featuring a Gaussian energy distribution and a focused spot radius of 20 μm. Generally, the thickness of the thermal barrier layer should not exceed 1 μm to avoid affecting antenna signal transmission. Therefore, for simulation, we selected an intermediate thickness of 500nm and first determined the optimal laser single-pulse energy ablation parameters. The pulse width was set to 120 ns, and single-pulse energies of 300 μJ, 350 μJ, 400 μJ and 450 μJ were simulated. Subsequently, under the optimized single-pulse energy, the thermal barrier layer thickness was systematically adjusted to 0 nm(No thermal barrier layer), 50 nm, 100 nm, 200 nm, 300 nm and 1 μm to determine the optimal value. Building on this, the effects of varying pulse widths (80 ns, 100 ns, 120 ns) and scanning speeds (250 mm/s, 300 mm/s, 350 mm/s, 400 mm/s) on laser ablation were investigated.

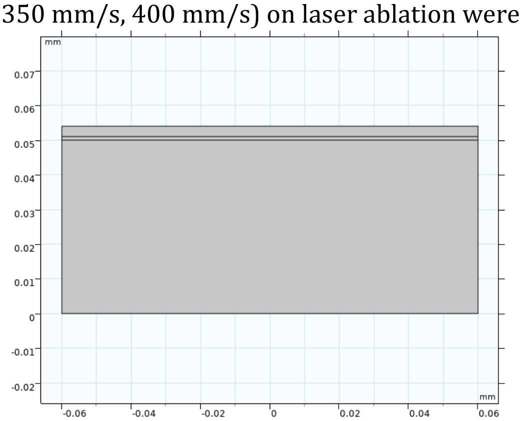

Figure 1. Schematic diagrams of Cu/Ti/PI models.

Through parameter optimization and literature review, the material properties of Cu, PI and Ti adopted for the simulation are summarized in Table 1Table 3. The computational domain was discretized using triangular mesh elements, with localized mesh refinement in the laser irradiation zone to ensure accuracy in transient temperature field calculations. To simplify the analysis, the following assumptions were made:

All materials are isotropic and remain perfectly bonded at the metal film/thermal barrier/PI substrate interfaces throughout the etching process.Energy dissipation occurs only through radiation and thermal convection; other forms of energy loss are neglected.

The primary removal mechanism is vaporization; splattering of molten metal and fluid dynamics effects are disregarded.Mechanical contributions to material delamination (e.g., stress-induced peeling) are not considered. Material is assumed to be fully removed once its vaporization temperature is reached.Upon reaching the vaporization temperature under pulsed laser irradiation, the material's thermophysical properties are replaced by those of air[16].

Table 1. Thermal physical properties of copper thin film.

Properties	Solid state	Liquid state
Density (kg/m3)	8960	8100
Specific heat (J/(kg·K))	385+0.045×(T−300)	560+0.015×(T−1357)
Heat conductivity (W/(m·K))	406-0.107×(T−300)	250−0.03×(T−1357)
Absorptivity	0.04	0.06
Melting point (K)	1357	/
Vaporization point (K)	/	2840

Table 2. Thermal physical properties of polyimide.

Material	Density (kg/m3)	Specific heat (J/(kg·K))	Heat conductivity (W/(m·K))	Vaporization point (K)
Polyimide	1300	1100	0.15	875

Table 3. Thermal physical properties of Titanium thin film.

Properties	Solid state	Liquid state
Density (kg/m3)	4510 - 0.4×(T - 300)	4200
Specific heat (J/(kg·K))	523 + 0.02×(T - 300)	650
Heat conductivity (W/(m·K))	22 - 0.005×(T - 300)	23
Melting point (K)	1668	/
Vaporization point (K)	/	3560

2.2. Heat Source Model

During the laser etching process, the laser energy is converted into the internal energy of copper, raising its temperature until vaporization occurs. The process adheres to Fourier's law of heat conduction and the principle of energy conservation. Based on the aforementioned assumptions, the heat conduction equation is expressed as follows[17]:

$$\rho c \frac{\partial T}{\partial t} = k\left(\frac{\partial^2 T}{\partial x^2} + \frac{\partial^2 T}{\partial y^2}\right) + Q \quad (1)$$

The initial temperature for all boundaries in the computational model was set to 20°C. The thermal convection at the model boundaries is described by:

$$q_0 = h\left(T_{\text{ext}} - T\right) \quad (2)$$

The thermal radiation at the model boundaries is given by:

$$-k\frac{\partial T}{\partial n}\Big|_{\Gamma} = \sigma\varepsilon\left(T_{\text{ext}}^4 - T^4\right) \quad (3)$$

Where T is the boundary temperature (K). Γ represents the boundary condition domain. q_0 denotes the convective heat flux. h is the convective heat transfer coefficient. n indicates the outward normal vector of the boundary. σ is the Stefan-Boltzmann constant. ε represents the material emissivity (dimensionless, taken as 0.04 in this study). Text is the ambient temperature (293 K, corresponding to 20°C initial condition)

The two-dimensional Gaussian laser beam profile is illustrated in Figure 2, demonstrating concentrated energy distribution at the center with rapid radial attenuation. The laser single-pulse energy is calculated according to the formula[18]:

$$E = \frac{P_{\text{ave}}}{f \cdot \tau} \tag{4}$$

The incident two-dimensional Gaussian laser beam profile is mathematically described as follows[19]:

$$S = (1 - R) \cdot \frac{3E}{\pi r^2} \cdot \exp\left(- \frac{3x^2}{r^2} \right) \cdot g(t) \tag{5}$$

The temporal profile of the pulsed laser loading can be mathematically represented as[20]:

$$g(t) = \begin{Bmatrix} 1, & 0 < t < \tau \\ 0, & \text{others} \end{Bmatrix} \tag{6}$$

The parameters can be represented as follows: R represents the material surface reflectivity. Pave denotes the average laser power. f indicates the laser repetition frequency. r specifies the laser beam spot radius. τ is the laser pulse width.

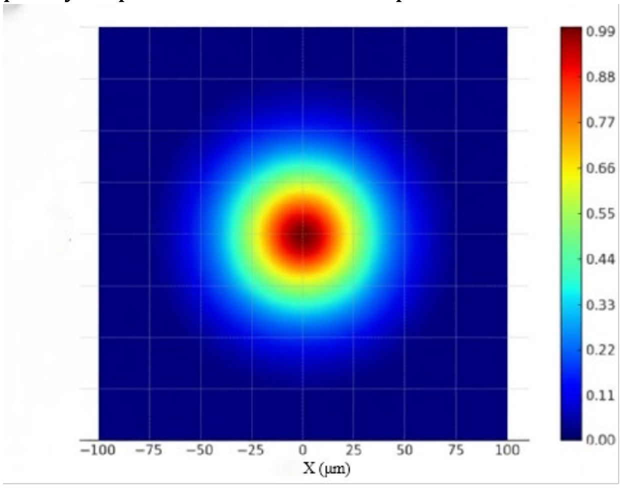

Figure 2. Schematic diagram of gaussian laser field intensity.

3. Analysis and Discussion

The primary mechanism of laser ablation is thermal ablation, wherein copper is removed through vaporization. In the finite element model, a laser heat source and solid heat transfer physics were defined. Under laser irradiation, heat was transferred to the copper material, causing its temperature to rise. A "filter" function was applied within the simulation software to remove material that reaches the vaporization temperature, thereby simulating the material removal process during laser ablation[21].

3.1. The effect of different single pulse energy

Under single-pulse energies of 300 μJ, 350 μJ, 400 μJ, and 450 μJ, the temperature distribution of laser ablation is illustrated in Figure 3 Analysis revealed that:
At 300 and 350 μJ (see Figure 3(a – b)), Cu removal was incomplete, with an ablation depth of 1.36 μm and 2.15 μm respectively. At 400 μJ (see Figure 3(c)), although Cu etching occurred, the bottom ablation width was limited to 4.54 μm. At 450 μJ (see Figure 3(d)), the bottom ablation width was 8.99 μJ, optimal ablation quality was achieved. Consequently, 450 μJ was selected for subsequent simulations investigating thermal barrier layer thickness variations.

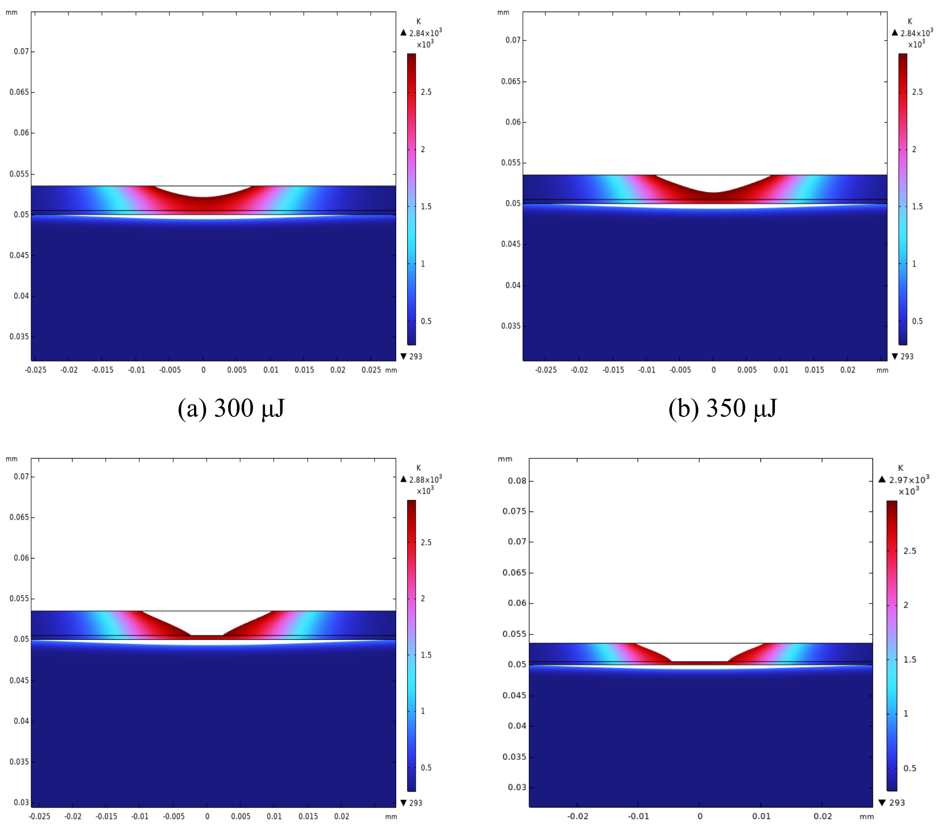

(a) 300 μJ (b) 350 μJ

(c) 400 μJ (d) 450 μJ

Figure 3. Thermal distribution maps of laser ablation under varying pulse energies. (a) 300 μJ, (b) 350 μJ, (c) 400 μJ and (d) 450 μJ.

3.2. Effect of different thermal barrier layer thickness

Next, a single pulse energy of 450 μJ with a pulse duration of 120 ns and a laser spot radius of 20 μm was selected for simulation. The laser ablation behavior of Cu and PI is shown in Figure 4. When the thermal barrier layer is absent (0 nm thick) (see Figure 5(a)), the ablation width at the bottom of the Cu film under a 450 μJ single pulse was 13.62 μm. After introducing the thermal barrier layer, the ablation widths at the bottom of the Cu corresponding to barrier thicknesses of 50 nm, 100 nm, 200 nm, 300 nm, 500 nm, and 1 μm were 13.11 μm, 12.75 μm, 11.97 μm, 11.15 μm, 8.99 μm, and 0 μm (no penetration), respectively. The excessively thick thermal barrier layer resulted in poor copper film removal. Meanwhile, the ablation width at the top of the Cu layer also decreased inversely with increasing barrier layer thickness.

This phenomenon is attributed to changes in the overall thermal properties, which alter the heat distribution and transfer mechanisms. Under constant conditions except for the introduction of the thermal barrier layer between the copper film and the PI layer, the thermal conductivity of titanium (~22 W/(m·K)) is significantly higher than that of polyimide (PI) (~0.1-0.2 W/(m·K)). In the original Cu/PI bilayer structure, the low thermal conductivity of the PI beneath the copper layer leads to heat accumulation within the copper during laser irradiation, facilitating the copper reaching its vaporization temperature and undergoing complete ablation. However, after introducing the titanium layer, heat generated in the copper film is more rapidly conducted into the titanium, thereby reducing thermal accumulation within the copper, decreasing its temperature rise rate, and making it difficult for the copper to reach the vaporization threshold[22]. Additionally, a significant interfacial thermal barrier may exist at the Cu/Ti interface, causing non-ideal thermal coupling, temperature gradient distortion, and localized hotspots, which further weaken heat transfer in the vertical direction within the copper layer, resulting in the copper bottom failing to reach the ablation temperature[23].

In summary, the introduction of the titanium barrier layer significantly alters the distribution and effects of laser energy within the material by influencing thermal conduction, interfacial coupling, mechanical response, and laser absorption. As a result, under the same single-pulse energy, the copper layer cannot be completely removed.

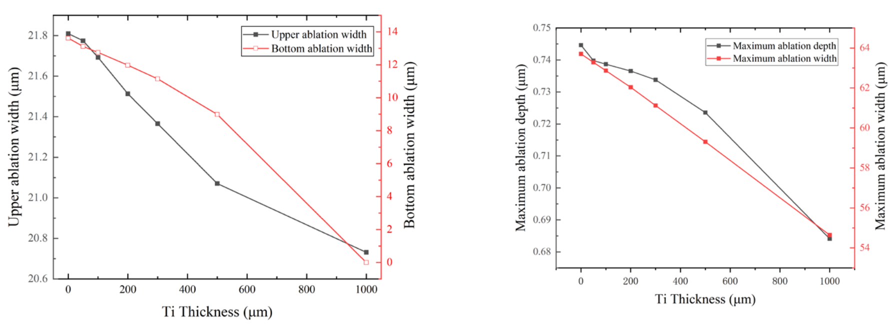

(a)Cu curve (b)PI curve

Figure 4. Ablation depth and width curves of Cu/Ti/PI layers under 450 μJ single-pulse energy. (a) Cu curve and (b) PI curve.

As the temperature diffuses downward, although the intermediate Ti layer does not reach its vaporization temperature, the temperature of the PI layer exceeds its vaporization threshold. As shown in Figure 5(b-f) and Figure 3(d), the region of the PI substrate reaching the vaporization threshold forms a flattened triangular area. The maximum depths within the PI layer reaching the vaporization threshold corresponding to barrier layer thicknesses of 50 nm, 100 nm, 200 nm, 300 nm, 500 nm, and 1 μm are 739.8 nm, 738.7 nm, 736.5 nm, 733.8 nm, 723.6 nm, and 684.1 nm, respectively. Compared to the maximum ablation depth of 744.6 nm for the no thermal barrier structure, these represent reductions of 0.65%, 0.80%, 1.09%, 1.46%, 2.83%, and 8.13%, respectively. The maximum widths of the PI layer reaching the vaporization threshold are 63.28 nm, 62.86 nm, 62.03 nm, 61.12 nm, 59.31 nm, and 54.65 nm, respectively, which correspond to decreases of 0.66%, 1.32%, 2.62%, 4.06%, 6.91%, and 14.22% compared to the maximum ablation width of 63.71 nm for the Cu/PI bilayer structure(see Figure 5(a)).

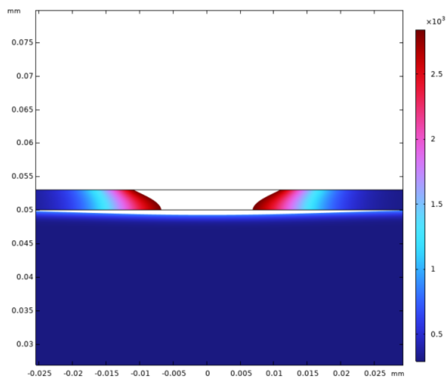

(a) 0 nm

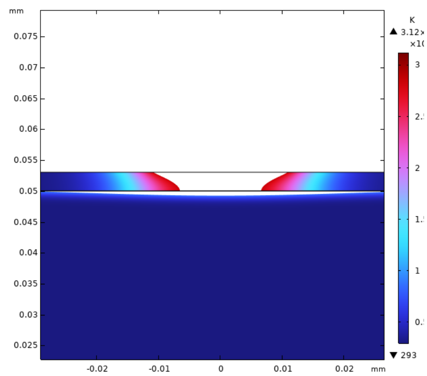

(b) 50 nm

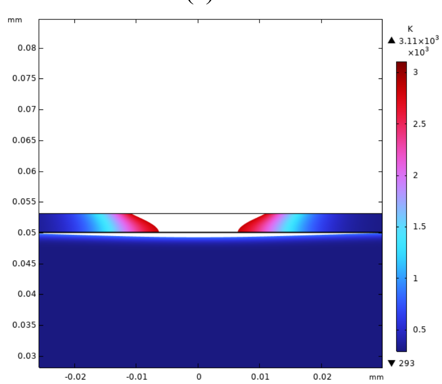

(c) 100 nm

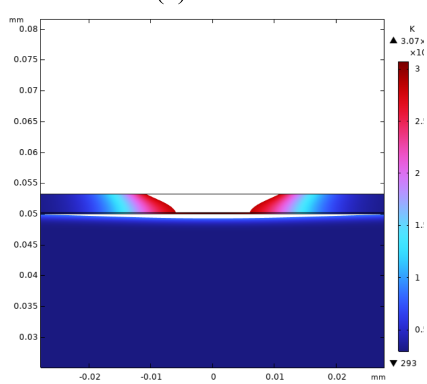

(d) 200 nm

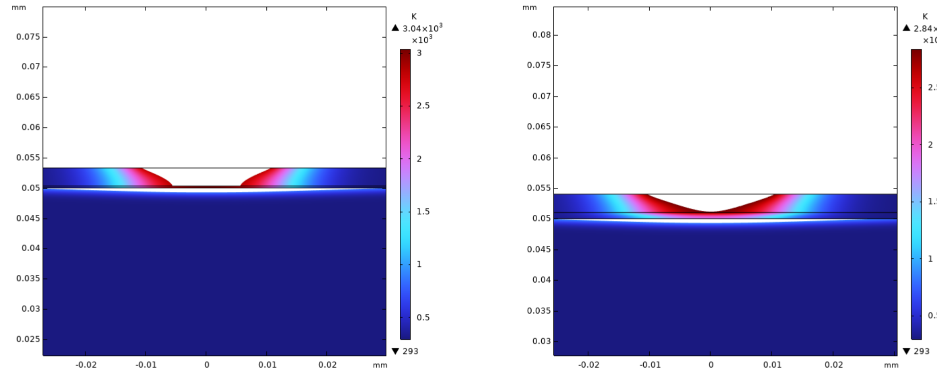

(e) 300 nm (f) 1 μm

Figure 5. Temperature distribution during single-pulse ablation with Ti layers of varying thicknesses. (a) 0 nm, (b) 50 nm, (c) 100 nm, (d) 200 nm, (e) 300 nm and (f) 1μm.

Figure 6 shows the temperature versus time curves at the center point of the Cu/PI interface line without a barrier layer and at the midpoint of the Ti/PI interface line with an added barrier layer, under irradiation with a single pulse of 450 μJ, 120 ns pulse duration, and a laser spot radius of 20 μm. As observed from the figure, When there is no thermal barrier layer, the center point on the upper PI layer first reaches the vaporization threshold at 25 ns, while the center point reaches the vaporization temperature of Cu at 107 ns, indicating that the laser directly irradiates the PI interface.

As shown in the lower left corner of the Figure 6, after introducing the barrier layer, the temperature at the midpoint of the Ti/PI interface line rises rapidly during the initial stage. When a thermal barrier layer such as Ti is inserted between Cu and PI, although the overall heat transfer to the PI is delayed, Ti's relatively low thermal conductivity causes part of the heat originating from the Cu layer to be temporarily retained near the interface during the early phase of laser irradiation. This results in rapid local heat accumulation at the PI surface, causing a faster temperature rise at the PI top. In contrast, without Ti, heat more readily diffuses into the interior of the PI, leading to a slower surface temperature increase. This phenomenon arises from a temporary "compression" of heat flux at the thermal barrier layer, creating a localized thermal concentration effect. Although overall vaporization is delayed, the accelerated surface temperature rise is due to the local heat storage effect of the Ti barrier layer, which also causes a transient "plateau" period that postpones heat conduction into the PI[24–25]. When the barrier layer thickness is 50 nm or 100 nm, the layer is too thin to sufficiently reduce the heat flow rate, resulting in a vaporization time for the PI close to that without the barrier. However, with increasing barrier thickness, the vaporization time of the PI is progressively delayed.

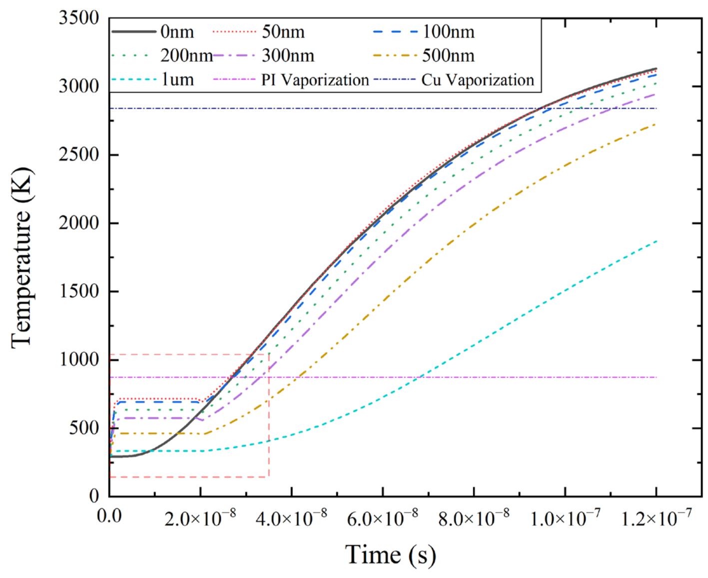

Figure 6. Temperature vs. time curve at the center point on the top surface of the PI substrate under single-pulse irradiation.

The Ti thermal barrier layer, due to its high vaporization temperature, did not reach its vaporization point under the 450 μJ single-pulse irradiation. However, when the barrier layer is relatively thin (below 100 nm), the PI layer can locally reach or exceed its vaporization temperature, resulting in the formation of a transient micro-vapor layer (or bubble layer). This generates localized pressure or expansion, which may lead to an "explosive" removal of the barrier layer, potentially exposing the underlying PI to direct laser irradiation prematurely[26]. Conversely, an overly thick barrier layer can negatively affect ablation efficiency. Under a 450 μJ single pulse, the bottom ablation width of the Cu layer with a 500 nm thick Ti barrier is only 8.99 μm, significantly reducing both the ablation efficiency and the taper angle. When the barrier layer thickness reaches 1 μm, the copper film is not ablated at all.

When the barrier layer thickness is 200 nm and 300 nm, the time required for the center point at the top of the PI layer to reach the vaporization threshold is 30 ns and 33 ns, respectively. Compared to 25 ns without a barrier layer, the vaporization is delayed by 5 ns and 8 ns. At the same time, there is no significant impact on the bottom ablation width of the copper film or the overall etching efficiency.In summary, when the titanium barrier layer thickness is in the range of 200–300 nm, it effectively delays the onset of PI vaporization while the high vaporization temperature of Ti helps prevent direct laser exposure to the PI surface.

3.3. Pulse Width

The common pulse widths of the laser are 80-120 ns. Based on the preliminary 120 ns pulse width, with a single pulse energy of 450 μJ and a thermal barrier layer thickness of 300 nm, the laser ablation effects under different pulse widths of 80 ns, 100 ns, and 120 ns were investigated, and the results are shown in Figure 7. Under the 80 ns pulse width, due to the short laser interaction time, the Cu layer was not removed, with a maximum ablation depth of 2.94 μm (see Figure 7(a)), indicating that a larger pulse width is required for complete removal. Figure 7(b) shows that under the 100 ns pulse width, the Cu layer was effectively removed, with an upper removal width of 21.84 μm and a bottom removal width of 9.15 μm. The maximum depth of the flattened triangular region in the PI layer reaching the vaporization threshold was 719.7 nm, with a maximum width of 59.89 μm. Compared to the results under the 120 ns pulse width (see Figure 5(d)), the bottom removal width of Cu decreased by 17.94% from 11.15 μm, the maximum depth of the flattened triangular region in the PI layer reaching the vaporization threshold decreased by 1.92% from 733.8 nm, and the maximum width decreased by 2.01% from 61.12 μm. The shorter pulse width reduces the etching efficiency of Cu, while the impact on the PI layer is almost negligible. Therefore, compared to 80 ns and 100 ns, the 120 ns pulse width provides the optimal etching efficiency.

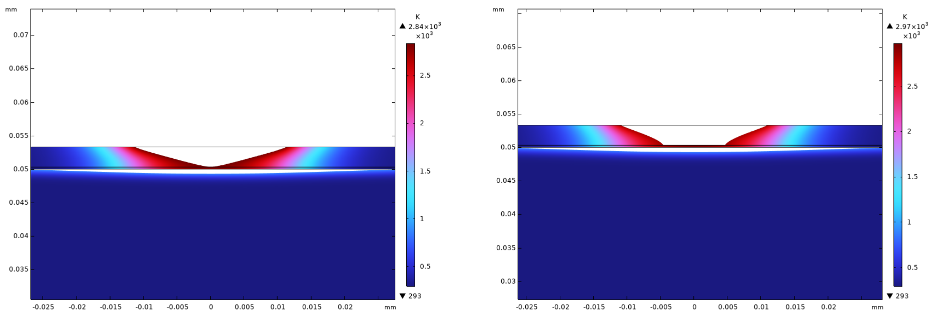

(a) 80ns (b) 100ns

Figure 7. Effect of laser ablation under different pulse width. (a)80ns and (b)100ns.

3.4. Scanning Speed

The scanning speed directly affects the etching quality of the material surface; therefore, it is essential to control the scanning speed appropriately. The relationship between scanning speed and the overlap ratio of adjacent laser spots is given by[27]:

$$\eta = \left(1 - \frac{v}{D \cdot f}\right) \times 100\% \tag{7}$$

In the equation: η represents the laser spot overlap ratio, v is the laser scanning speed, D is the diameter of the focused square laser spot, f is the repetition frequency of the pulsed laser.

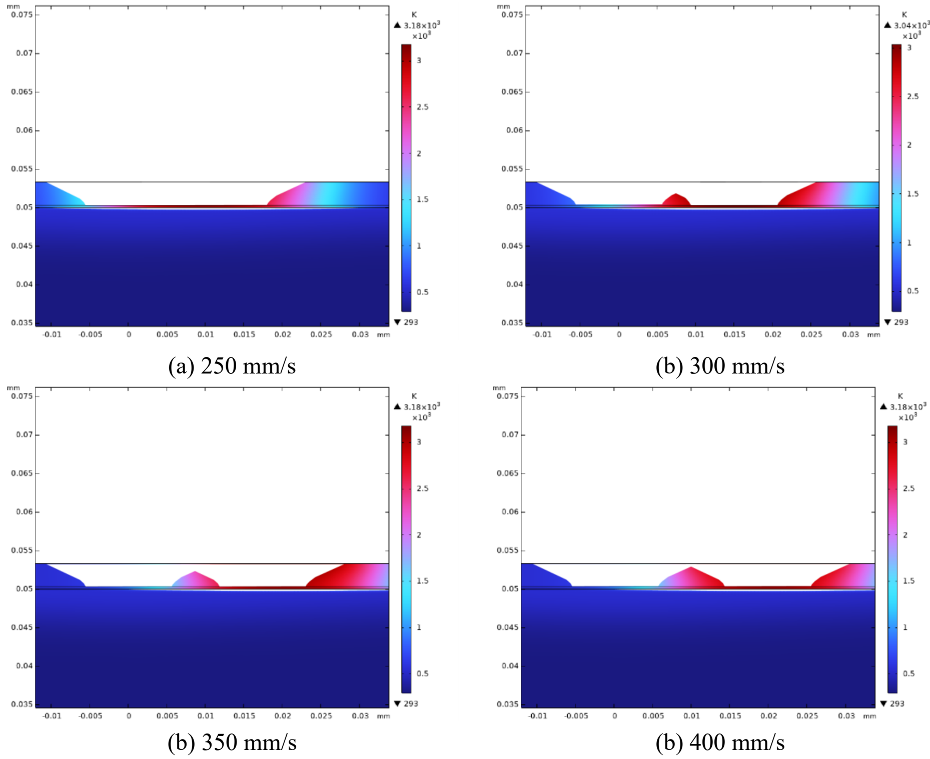

Figure 8. Temperature distribution under different scanning speeds. (a) 200 mm/s, (b) 300 mm/s, (c) 350 mm/s and (d) 400 mm/s.

Using the previously optimized simulation parameters—single-pulse energy of 450 μJ, pulse duration of 120 ns, laser spot radius of 20 μm, and thermal barrier layer thickness of 300 nm—simulations were conducted by varying the laser scanning speed. Four scanning speeds were selected: 250 mm/s, 300 mm/s, 350 mm/s, and 400 mm/s. The simulation results are shown in Figure 8. At a scanning speed of 250 mm/s, the calculated spot overlap ratio based on Equation (6) is 68.75%. As shown in Figure 8(a), the copper layer is cleanly removed with a smooth surface, indicating an ideal ablation result. In comparison, at scanning speeds of 300 mm/s (see Figure 8(b)) and 350 mm/s (see Figure 8(c)), the corresponding overlap ratios are 62.50% and 56.25%, respectively. As the scanning speed increases, the overlap ratio decreases, leading to degraded surface removal quality. Gaps between pulses resulted in unetched regions. Specifically, at 300 mm/s, a raised ridge with a height of 1.55 μm and a width of 3.84 μm is observed; at 350 mm/s, the ridge height increases to 2.12 μm and the width to 6.34 μm.When the scanning speed reaches 400 mm/s (see Figure 8(d)), the overlap ratio drops to 50%, producing the poorest etching performance. A prominent raised ridge with a height of 2.67 μm and a width of 8.83 μm is observed, and large unablated regions remain due to the insufficient overlap between pulses.In summary, under the conditions of a single-pulse energy of 450 μJ, a 300 nm-thick thermal barrier layer, and a scanning speed of 250 mm/s, the best ablation quality is achieved. However, in practical scanning processes, high overlap ratios can intensify thermal accumulation in the PI substrate[28]. To mitigate potential thermal damage to the PI, it is advisable to adopt interlaced scanning patterns or employ delayed pulse strategies during processing[29].

4. Conclusion

The finite element simulation of laser ablation on the Cu/Ti/PI trilayer structure reveals that the introduction of a titanium thermal barrier layer significantly influences heat transfer and ablation characteristics. A Ti layer thickness of 200 – 300 nm optimally delays the vaporization of the underlying PI substrate without compromising copper removal efficiency. The pulse width of 120 ns and scanning speed of 250 mm/s were found to yield the best ablation quality, ensuring complete copper film removal while minimizing thermal damage to the PI. These findings provide a theoretical basis for optimizing laser processing parameters in the fabrication of flexible electronic devices with multilayer film structures.

Acknowledgements

This work was supported by Vacuum Technology and Physics Laboratory (Lanzhou Institute of Physics) (HTKJ2023KL510004), 111 project of China (D21017), Shandong Provincial Key Research and Development Program (International Science and Technology Cooperation) (No. 2024KJHZ002), Natural Science Foundation of Shandong Province (No. ZR2023ME156), “Double Hundred Plan” Talent Program of Shandong Province (WSR2023055), National Natural Science Foundation of China (52405492) and Qingdao Natural Science Foundation (24-4-4-zrjj-68-jch).

References

[1] Anwar, R., Mao, L., & Ning, H. (2018). Frequency Selective Surfaces: A Review. Applied Sciences, 8(9), 1689. https://doi.org/10.3390/app8091689

[2] Usmani, W. U., Chietera, F. P., & Mescia, L. (2025). Flexible Phased Antenna Arrays: A Review. Sensors, 25(15), 4690. https://doi.org/10.3390/s25154690

[3] Gal-Katziri, M., Fikes, A., & Hajimiri, A. (2022). Flexible active antenna arrays. Npj Flexible Electronics, 6(1). https://doi.org/10.1038/s41528-022-00218-z

[4] Dong, Z., He, Q., Shen, D., Gong, Z., Zhang, D., Zhang, W., Ono, T., & Jiang, Y. (2023). Microfabrication of functional polyimide films and microstructures for flexible MEMS applications. Microsystems & Nanoengineering, 9(1). https://doi.org/10.1038/s41378-023-00503-5

[5] Zhang, C., He, X., & Lu, Q. (2024). High-frequency low-dielectric-loss in linear-backbone-structured polyimides with ester groups and ether bonds. Communications Materials, 5(1). https://doi.org/10.1038/s43246-024-00502-7

[6] Kirtania, S. G., Elger, A. W., Hasan, Md. R., Wisniewska, A., Sekhar, K., Karacolak, T., & Sekhar, P. K. (2020). Flexible Antennas: A Review. Micromachines, 11(9), 847. https://doi.org/10.3390/mi11090847

[7] Shin, B. S., Oh, J. Y., & Sohn, H. (2007). Theoretical and experimental investigations into laser ablation of polyimide and copper films with 355-nm Nd:YVO4 laser. Journal of Materials Processing Technology, 187 – 188, 260 – 263. https://doi.org/10.1016/j.jmatprotec.2006.11.106

[8] Mamleyev, E. R., Heissler, S., Nefedov, A., Weidler, P. G., Nordin, N., Kudryashov, V. V., Länge, K., MacKinnon, N., & Sharma, S. (2019). Laser-induced hierarchical carbon patterns on polyimide substrates for flexible urea sensors. Npj Flexible Electronics, 3(1). https://doi.org/10.1038/s41528-018-0047-8

[9] Wang, R., Gesang, D. Z., Wei, G., Yang, J. P., Hu, H., Shang, K., & Wu, G. (2024). Study on pulse laser etched interface characteristics of metal thin film/organic material structures for space antennas. Vacuum and Cryogenics, 30(5), 522 – 527.

[10] Linden, J., Hoch, A., Levy, A., Sakaev, I., Toker, G. B., Fogel, O., Hod, M., & Zalevsky, Z. (2022). Enhanced throughput and clean laser drilling with a sacrificial polymer layer. Optical Materials Express, 12(12), 4682. https://doi.org/10.1364/ome.467696

[11] Hribar, L., Gregorčič, P., Senegačnik, M., & Jezeršek, M. (2022). The Influence of the Processing Parameters on the Laser-Ablation of Stainless Steel and Brass during the Engraving by Nanosecond Fiber Laser. Nanomaterials, 12(2), 232. https://doi.org/10.3390/nano12020232

[12] He, Z., Lei, L., Lin, S., Tian, S., Tian, W., Yu, Z., & Li, F. (2024). Metal Material Processing Using Femtosecond Lasers: Theories, Principles, and Applications. Materials, 17(14), 3386. https://doi.org/10.3390/ma17143386

[13] Deng, G., Xie, J., Ling, H., Hu, A., & Li, M. (2025). Preparation methods and performance study of high conductivity and low roughness copper platings. Plating and Finishing, 47(3), 18 – 25.

[14] Cahill, D. G., Ford, W. K., Goodson, K. E., Mahan, G. D., Majumdar, A., Maris, H. J., Merlin, R., & Phillpot, S. R. (2003). Nanoscale thermal transport. Journal of Applied Physics, 93(2), 793 – 818. https://doi.org/10.1063/1.1524305

[15] Sidambe, A. T., Tian, Y., Prangnell, P. B., & Fox, P. (2019). Effect of processing parameters on the densification, microstructure and crystallographic texture during the laser powder bed fusion of pure tungsten. International Journal of Refractory Metals and Hard Materials, 78, 254 – 263. https://doi.org/10.1016/j.ijrmhm.2018.10.004

[16] Lim, H. S., & Yoo, J. (2011). FEM based simulation of the pulsed laser ablation process in nanosecond fields. Journal of Mechanical Science and Technology, 25(7), 1811 – 1816. https://doi.org/10.1007/s12206-011-0511-z

[17] Miao, R., Wang, T., Yao, T., Hu, S., Huang, X., & Kang, Q. (2021). Experimental and numerical simulation analysis of laser paint removal of aluminum alloy. Journal of Laser Applications, 34(1). https://doi.org/10.2351/7.0000522

[18] Long, R. S., Liu, W. J., & Shang, X. F. (2007). Numerical simulation of temperature field on laser metal deposition shaping. Laser Technology, 31(4), 394 – 396, 430.

[19] Yang, J., Zhou, J., Sun, Q., Meng, X., Guo, Z., & Zhu, M. (2021). Digital analysis and prediction of the topography after pulsed laser paint stripping. Journal of Manufacturing Processes, 62, 685 – 694.

[20] Yang, T. (2022). Simulation study and experimental verification of laser surface removal of carbon fiber composites [Master's thesis, Civil Aviation Flight School of China].

[21] Gao, L., Zhou, J., Sun, Q., Li, H., Zhu, M., Guo, Z., & Yang, J. (2019). Numerical simulation and surface morphology of laser-cleaned aluminum alloy paint layer. Chinese Journal of Lasers, 46(5), 0502002.

[22] Kim, Y. W. (2002). Thermal Diffusivity Measurement for Titanium Thin Films on Copper Substrate by Laser Produced Plasmas. International Journal of Thermophysics, 23(4), 1091 – 1101. https://doi.org/10.1023/a:1016346221082

[23] Kim, B., Nam, H. K., Watanabe, S., Park, S., Kim, Y., Kim, Y.-J., Fushinobu, K., & Kim, S.-W. (2020). Selective Laser Ablation of Metal Thin Films Using Ultrashort Pulses. International Journal of Precision Engineering and Manufacturing-Green Technology, 8(3), 771 – 782. https://doi.org/10.1007/s40684-020-00272-w

[24] Tsibidis, G. D. (2014). Thermal response of double-layered metal films after ultrashort pulsed laser irradiation: the role of nonthermal electron dynamics. arXiv.

https://doi.org/10.48550/ARXIV.1402.1274

[25] Chiang, D., Tseng, S. F., Hsiao, W. T., & Hsiao, C. N. (2012). Temperature profile of the multilayer structure irradiated by pulsed laser. Applied Physics A, 110(3), 571 – 578. https://doi.org/10.1007/s00339-012-7129-6

[26] Hong, J., Cheng, P., Guo, J., Chen, W., Li, Y., Liu, J., Zhu, Q., & Chen, J. (2023). The mechanism study of laser peeling of ultra-thin polyimide film from the transparent substrate. Surfaces and Interfaces, 36, 102561. https://doi.org/10.1016/j.surfin.2022.102561

[27] Jasim, H. A., Demir, A. G., Previtali, B., & Taha, Z. A. (2017). Process development and monitoring in stripping of a highly transparent polymeric paint with ns-pulsed fiber laser. Optics & Laser Technology, 93, 60 – 66. https://doi.org/10.1016/j.optlastec.2017.01.031

[28] Wang, R., Wang, Y., Yang, Y., Zhang, S., Liu, Y., Yao, J., & Zhang, W. (2023). A Systematic Study on the Processing Strategy in Femtosecond Laser Scribing via a Two-Temperature Model. Materials, 16(21), 6895. https://doi.org/10.3390/ma16216895

[29] Moskal, D., Martan, J., & Honner, M. (2023). Scanning Strategies in Laser Surface Texturing: A Review. Micromachines, 14(6), 1241. https://doi.org/10.3390/mi14061241